Astronomy & Astrophysics

Three Saturn-mass planets transiting F-type stars revealed with TESS and HARPS

TOI-615b, TOI-622b, and TOI-2641b[★]

Angelica Psaridi[1], François Bouchy[1], Monika Lendl[1], Babatunde Akinsanmi[1], Keivan G. Stassun[2],
Barry Smalley[3], David J. Armstrong[4,5], Saburo Howard[6], Solène Ulmer-Moll[1,7], Nolan Grieves[1],
Khalid Barkaoui[8,9,10], Joseph E. Rodriguez[11], Edward M. Bryant[12], Olga Suárez[6], Tristan Guillot[6],
Phil Evans[13], Omar Attia[1], Robert A. Wittenmyer[14], Samuel W. Yee[15], Karen A. Collins[16],
George Zhou[14], Franck Galland[1,17], Léna Parc[1], Stéphane Udry[1], Pedro Figueira[1,18], Carl Ziegler[19],
Christoph Mordasini[7], Joshua N. Winn[15], Sara Seager[9,20,21], Jon M. Jenkins[27], Joseph D. Twicken[27,22],
Rafael Brahm[23,24,25], Matías I. Jones[26], Lyu Abe[6], Brett Addison[14,28], César Briceño[29],
Joshua T. Briegal[30], Kevin I. Collins[31], Tansu Daylan[15], Phillip Eigmüller[32],
Gabor Furesz[20], Natalia M. Guerrero[33,20], Janis Hagelberg[1], Alexis Heitzmann[14],
Rebekah Hounsell[34,35], Chelsea X. Huang[14], Andreas Krenn[1,36], Nicholas M. Law[37], Andrew W. Mann[37],
James McCormac[4,5], Djamel Mékarnia[6], Dany Mounzer[1], Louise D. Nielsen[38], Ares Osborn[4,5],
Yared Reinarz[24], Ramotholo R. Sefako[39], Michal Steiner[1], Paul A. Strøm[4,5], Amaury H. M. J. Triaud[40],
Roland Vanderspek[9,20], Leonardo Vanzi[41], Jose I. Vines[42], Christopher A. Watson[43],
Duncan J. Wright[14], and Abner Zapata[41]

(Affiliations can be found after the references)

ABSTRACT

While the sample of confirmed exoplanets continues to grow, the population of transiting exoplanets around early-type stars is still limited. These planets allow us to investigate the planet properties and formation pathways over a wide range of stellar masses and study the impact of high irradiation on hot Jupiters orbiting such stars. We report the discovery of TOI-615b, TOI-622b, and TOI-2641b, three Saturn-mass planets transiting main sequence, F-type stars. The planets were identified by the Transiting Exoplanet Survey Satellite (TESS) and confirmed with complementary ground-based and radial velocity observations. TOI-615b is a highly irradiated ($\sim$1277 $F_{\oplus}$) and bloated Saturn-mass planet ($1.69^{+0.05}_{-0.06}$ R_{Jup} and $0.43^{+0.09}_{-0.08}$ M_{Jup}) in a 4.66 day orbit transiting a 6850 K star. TOI-622b has a radius of $0.82^{+0.03}_{-0.03}$ R_{Jup} and a mass of $0.30^{+0.07}_{-0.08}$ M_{Jup} in a 6.40 day orbit. Despite its high insolation flux ($\sim$600 $F_{\oplus}$), TOI-622b does not show any evidence of radius inflation. TOI-2641b is a $0.39^{+0.02}_{-0.04}$ M_{Jup} planet in a 4.88 day orbit with a grazing transit (b = $1.04^{+0.05}_{-0.06}$) that results in a poorly constrained radius of $1.61^{+0.46}_{-0.64}$ R_{Jup}. Additionally, TOI-615b is considered attractive for atmospheric studies via transmission spectroscopy with ground-based spectrographs and JWST. Future atmospheric and spin-orbit alignment observations are essential since they can provide information on the atmospheric composition, formation, and migration of exoplanets across various stellar types.

Key words. planets and satellites: individual: TOI-615b – planets and satellites: individual: TOI-622b – stars: early-type – techniques: photometric – techniques: radial velocities – planets and satellites: individual: TOI-2641b

1. Introduction

To date, more than 122 extrasolar planets with well-constrained densities[1] that are transiting AF-type, main-sequence stars above the Kraft break ($T_{\mathrm{eff}} \gtrsim 6200$ K, $\lesssim$ F8V, or $M_* \gtrsim 1.1$ $M_{\odot}$; Kraft 1967) have been discovered according to the PlanetS exoplanet catalog[2] (Otegi et al. 2020). Obtaining mass measurements of

planets orbiting such stars is inherently more difficult than for Solar-type stars. These stars have thin convective envelopes, do not efficiently generate magnetic winds, and often rotate rapidly. Consequently, they exhibit broader and fewer spectral lines due to their rapid rotation and high temperature, complicating high precision radial velocity (RV) measurements.

Hot Jupiters that closely orbit early-type stars are scientifically interesting since their high equilibrium temperatures make them valuable for atmospheric characterization via transmission spectroscopy. Additionally, 20 out of the 35 planets on misaligned orbits ($|\lambda| > 10°$, with >3σ confidence) have been found to orbit stars with effective temperatures above the Kraft break (DACE[2]). Their high obliquities, compared to planets orbiting cooler stars (Winn et al. 2010), can provide insight into the formation of the system, suggesting that the planets were

---

[1] $\sigma_{\mathrm{M}}/\mathrm{M} \leq 25\%$ and $\sigma_{\mathrm{R}}/\mathrm{R} \leq 8\%$, resulting in density uncertainty $\leq 20\%$.
[2] Available on the Data & Analysis Center for Exoplanets (DACE) platform (https://dace.unige.ch).

formed ex situ and migrated inward due to interactions with the protoplanetary disk.

NASA's Transiting Exoplanet Survey Satellite (TESS, Ricker et al. 2015), in contrast to *Kepler* (Borucki et al. 2010), is focusing on bright targets including hot, early-type stars. TESS has delivered over 350 planetary candidates around stars with effective temperatures above the Kraft break so far – these objects necessitate further spectroscopic and photometric observations to confirm their planetary nature. To date, 25 exoplanets around early-type stars have been confirmed with such follow-up studies: HD 202772Ab (Wang et al. 2019), HD 2685b (Jones et al. 2019), TOI-150b, TOI-163b (Kossakowski et al. 2019), TOI-677b (Jordán et al. 2020), TOI-892b (Brahm et al. 2020), HD 5278b (Sozzetti et al. 2021), TOI-628b, TOI-640b, TOI-1333b (Rodriguez et al. 2021), TOI-1431b (Addison et al. 2021), TOI-201b (Hobson et al. 2021), TOI-2109b (Wong et al. 2021), TOI-3362b (Dong et al. 2021), TOI-1107b (Psaridi et al. 2022), TOI-1516b, TOI-2046b (Kabáth et al. 2022), TOI-1842b (Wittenmyer et al. 2022), TOI-4137b (Yee et al. 2022), TOI-5153b (Ulmer-Moll et al. 2022), TOI-558b (Ikwut-Ukwa et al. 2022), TOI-2152b, TOI-2154b, TOI-2497b (Rodriguez et al. 2023), and TOI-2803Ab (Yee et al. 2023).

Given the interest in understanding the planet formation process over a wide range of stellar characteristics and especially for massive stars, we began a survey characterizing TESS candidates around a sample of AF main-sequence stars with ground-based follow-up spectroscopy. Our target list consists of relatively bright stars ($V \leq 12$ mag) with effective temperatures above the Kraft break that host giant exoplanet and brown dwarf candidates ($R > 5R_\oplus$). This survey resulted in the detection of a new massive planet, TOI-1107b, and three brown dwarfs, TOI-629b, TOI-1982b, and TOI-2543b (Psaridi et al. 2022). In this work, we report the discovery and confirmation of three new Saturn-mass planets, TOI-615b, TOI-622b, and TOI-2641b, orbiting around F-type stars. The planets were initially detected in the TESS data during the first 3 yr of its mission (Sectors 1–39). In addition, we performed follow-up spectroscopic observations with HARPS, CORALIE and CHIRON, MINERVA-Australis, FIDEOS, and NRES, and ground-based photometry with EulerCam, NGTS, ASTEP, LCOGT, and El Sauce.

The paper is structured as follows: in Sect. 2 we describe the photometric and follow-up spectroscopic observations. Section 3 details the stellar characterization and the global analysis. Finally, in Sect. 4 we discuss the planets in context and the feasibility for future studies.

2. Observations

2.1. Photometry

The transits of the three targets were initially observed and detected in TESS photometry during the first 3 yr of its mission (Sectors 1–39). Afterward, we ruled out nearby eclipsing binaries (NEBs), confirmed the transit depth and refined the ephemeris with follow-up photometry as part of the TESS Follow-up Observing Program (TFOP, Collins et al. 2018). The summary of the photometric observations can be found in Table 1. All the light curves are presented in Fig. A.1.

2.1.1. TESS photometry

TOI-615 (TIC 190496853) was observed in Sectors 8 and 9 with a 30-min cadence and Sector 35 with a 2-min cadence. Nine

Table 1. Summary of the TESS and ground-based photometric observations of TOI-615, TOI-622, and TOI-2641.

Date(s)	Facility	Detrending
TOI-615		
2019 Feb 02–Mar 26	TESS FFI	–
2021 Feb 09–Mar 07	TESS 2-min	GPs
2020 Feb 07	El Sauce (B)	$p(AM)$
2021 Mar 18	ASTEP (R_c)	-
2022 Feb 16	EulerCam (V)	$p(AM + sky^2)$
TOI-622		
2019 Feb 02–Mar 26	TESS 2-min	GPs
2021 Jan 13–Mar 07	TESS 2-min	GPs
2019 Dec 22	NGTS[1]	$p(y^2 + FWHM)$
2019 Dec 22	NGTS[2]	$p(x + y^2 + FWHM)$
TOI-2641		
2021 Mar 07–Apr 20	TESS 2-min	GPs
2022 Feb 28	EulerCam (V)	$p(t + x)$
2021 May 26	LCOGT (g')	$p(sky)$
2021 May 26	LCOGT (i')	–
2021 May 21	LCOGT (i')	$p(t)$

Notes. The notation of the baseline models for, $p(j^i)$, refers to a polynomial of degree i in parameter j (t:time, AM:airmass, FWHM:stellar FWHM and sky:sky background). The notation of GPs refers to Gaussian Processes.

transits were detected in the Full Frame Images (FFIs) and four transits in the 2-min cadence light curves with a transit depth of ~1.12% and an average period of 4.66 days. TOI-615 passed all the Science Processing Operations Center (SPOC; Jenkins et al. 2016) Data Validation (DV) tests (Twicken et al. 2018, Li et al. 2019) and the difference image centroiding analysis for Sector 35 that located the transit signature source to within $0.7 \pm 2.5''$ of the target star.

TOI-622 (TIC 83092282) was observed in Sectors 8, 9, 34, and 35 at 2-min cadence where 14 transits were detected with a depth of ~0.38% and a period of 6.4 days. The transit signature passed all DV tests and the difference image centroid offsets for the four available Sectors located the source of the transits to within $1.5 \pm 2.5''$ of the target star.

Finally, TOI-2641 (TIC 162802770) was monitored in Sectors 36 and 37 at 2-min cadence. Nine transits with an orbital period of 4.88 days and a depth of ~0.28% were identified in the data, suggesting a ~6.9 $R_\oplus$ companion radius. The candidate passed all DV tests and the difference image centroid offsets for Sectors 36–37 located the source of the transits to within $2.1 \pm 2.7''$ of the target star. In Sect. 3.2, we show that the impact parameter is greater than one and the planetary radius is much larger than the initial estimate. The high impact parameter and the V-shaped transits suggest that the companion is in a highly grazing transit.

The 2-min cadence photometry is extracted by the SPOC pipeline which produces the Simple Aperture Photometry (SAP) flux and the Presearch Data Conditioning SAP (PDCSAP; Smith et al. 2012, Stumpe et al. 2012, 2014) flux. The 30-min photometry was produced by the MIT Quick Look Pipeline (QLP; Huang et al. 2020). The SPOC pipeline transiting planet search component employs an adaptive, noise-compensating matched filter (Jenkins 2002, 2010, 2020). The QLP searches light curves for periodic transits with the box-least-squares algorithm (BLS; Kovács et al. 2002). Alerts for planet candidate TOIs

(Guerrero et al. 2021) are issued by the TESS Science Office after vetting the SPOC and QLP transit detections.

2.1.2. Ground-based follow-up photometry

We observed a full transit of TOI-615 and TOI-2641 in V-band using the EulerCam instrument (Lendl et al. 2012) installed on the 1.2-m *Leonhard Euler* Telescope at ESO's La Silla Observatory. TOI-615 was observed on 2022 February 16 with an exposure time of 90 s and a defocus of 0.12 mm. TOI-2641 was observed on 2022 February 28 with an exposure time of 75 s and a defocus of 0.08 mm. We reduced the data with the standard procedure of bias subtraction and flat correction. For the reduction of the light curves we performed differential aperture photometry with a careful selection of aperture radius and comparison stars that minimize the RMS scatter in the out of transit portion.

TOI-622b was observed with the Next Generation Transit Survey (NGTS; Wheatley et al. 2018) on 2019 December 22. NGTS is a wide-field photometric survey installed at ESO's Paranal observatory in Chile that consists of an array of twelve individual robotic 20 cm telescopes, and by using multiple telescopes to simultaneously observe the same star can achieve high precision photometry for bright stars (Smith et al. 2020; Bryant et al. 2020). Two telescopes were used simultaneously covering the ingress and mid part of the transit with the custom NGTS filter (520–890 nm). A total of 2421 images were collected with an exposure time of 10 s. A custom aperture photometry pipeline, which uses the SEP Python library (Bertin & Arnouts 1996; Barbary 2016) to perform the source extraction and photometry, was used to reduce the NGTS data. During this reduction, comparison stars which are similar to TOI-622 in brightness, color and CCD position are automatically selected using *Gaia* DR2 (Gaia Collaboration 2018).

We observed three full transits of TOI-2641 using the Las Cumbres Observatory Global Telescope (LCOGT; Brown et al. 2013) 1.0-m network node at Cerro Tololo Interamerican Observatory. The telescope is equipped with 4096 × 4096 SINISTRO Cameras having an image scale of 0.389 arcsec pixel⁻¹, resulting in a 26′ × 26′ field of view. We used the TESS Transit Finder (TTF), which is a customized version of the Tapir software package (Jensen 2013), to schedule our transit observations. The first transit was observed on 2021 May 21 in the Sloan-i′ filter with an exposure time of 16s and a photometric aperture radius of 3.5 arcsec (9 pixel). Second and third transits were observed on UTC 2021 May 26 in the Sloan-′i and Sloan-g′ and a photometric aperture radius of 4.3 arcsec (11 pixel). The science images were calibrated (bias and dark subtraction and flat division) by the standard LCOGT BANZAI pipeline (McCully et al. 2018), and photometric measurements were extracted using AstroImageJ (Collins et al. 2017). A transit-like event consistent with the SPOC-reported event is detected in all three light curves. The follow-up apertures exclude flux from all known *Gaia* DR3 and TIC version 8 neighbors, except TIC 940863891, which is 3.″4 northwest of TOI-2641. However, it is fainter than TOI-2641 by 6.77 magnitudes, so is nominally too faint to be capable of producing the ∼2.7 ppt event in the SPOC photometric aperture. Nevertheless, we also extracted a light curve from 2021 May 21 observation using a smaller 2.″0 target aperture, which excluded most of the flux from the 3.4″ neighbor, and also detect a consistent event on-target although with lower photometric precision.

We observed a partial transit of TOI-615 on 2021 March 18, with the Antarctica Search for Transiting ExoPlanets (ASTEP) program (Guillot et al. 2015; Mékarnia et al. 2016). The 0.4 m

robotic telescope, located at Concordia station (Dome C, Antarctica) , is equipped with an FLI Proline KAF-16801E, 4096 × 4096 pixel CCD camera, observing in a roughly Rc band-pass with a 1° × 1° field of view. Due to the extremely low data transmission rate at the Concordia station, the data are processed on-site using an automated IDL-based pipeline described in Abe et al. (2013). The raw light curves of about 1000 stars are transferred to Europe on a server in Rome, Italy, and are then available for deeper analysis. These data files contain each star's flux computed through 10 fixed circular aperture radii so that optimal light curves can be extracted. For TOI-615 a 8.4 arcsec radius aperture gave the best result.

An egress of TOI-615 was observed on 2020 February 07 in Johnson B-band using the Evans 0.36 m telescope at El Sauce Observatory in Coquimbo Province, Chile. The telescope is equipped with a STT 1603-3 CCD camera with 1536 × 1024 pixels binned 2 × 2 in-camera resulting in an image scale of 1.47″ pixel⁻¹. The photometric data were obtained from 311 × 75 s exposures, after standard calibration, using a circular 7.4″ aperture in AstroImageJ (Collins et al. 2017).

2.2. Spectroscopy

2.2.1. Reconnaissance spectroscopy

We collected high resolution, low precision spectra of TOI-615 and TOI-622 that ruled out false positive scenarios, such as blended eclipsing binaries and starspots (Queloz et al. 2001a). The reconnaissance measurements are not precise enough to help constrain the planetary parameters, and so we do not include them in the global analysis.

TOI-615 was observed 33 times between 2019 December 06 and 2021 April 30 with CHIRON spectrograph (see Sect. 2.2.2) with an exposure time of 1000 s which translated in spectra with a signal-to-noise ratio per resolution element (S/N) between 29 and 77. The RV RMS is 155 m s⁻¹ and the mean measurement error is 140 m s⁻¹, which is ∼3.3 times the RV semi-amplitude of TOI-615b.

We obtained 56 reconnaissance spectra for TOI-622 between 2019 April 16 and 2021 January 12 using the MINERVA-Australis telescope array (Addison et al. 2019), located at Mt. Kent Observatory, Australia. Minerva-Australis is an array of four identical 0.7 m telescopes linked via fiber feeds to a single KiwiSpec echelle spectrograph at a spectral resolving power of $R \sim 80\,000$ over the wavelength region of 5000–6300 Å. Radial velocities for the observations are derived for each telescope by cross-correlation, where the template being matched is the mean spectrum of each telescope. Each epoch consists of 30–60 min exposures from up to four individual telescopes; the concurrent radial velocities from multiple telescopes are binned into a single point after accounting for the offsets between telescopes. The RV RMS is 106 m s⁻¹ and the average measurement error is 151 m s⁻¹ corresponding to ∼5.4 times the semi-amplitude of TOI-622b. We collected 12 spectra using Fiber Dual Echelle Optical Spectrograph (FIDEOS; Vanzi et al. 2018) spectrograph mounted on the ESO 1.0 m telescope at La Silla Observatory. The observations were obtained between 2019 May 15 and 2020 February 22 with an exposure time of 1200 s resulting in a S/N between 56 and 94. The RV RMS is 42 m s⁻¹ and the mean measurement error is 40 m s⁻¹ (∼1.4 times the RV semi-amplitude of TOI-622b). Additionally, we obtained 10 observations of TOI-622 from 2019 October 08 to 2019 November 02 with the Network of Robotic Echelle Spectrographs (NRES; Siverd et al. 2018) on the Las Cumbres Observatory (LCOGT;
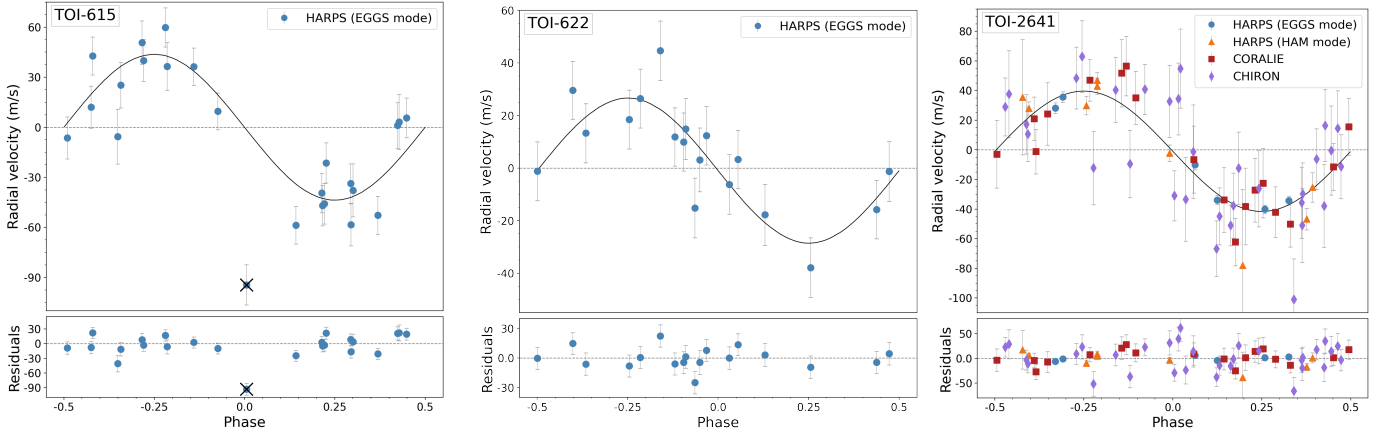
Fig. 1. Relative RVs of TOI-615 (*left*), TOI-622 (*middle*), and TOI-2641 (*right*). The different colors indicate different instruments. The black line shows the model fit derived with CONAN. The residuals of the model fit are shown in the *bottom panels*. For TOI-615 the crossed-out HARPS data point was collected during transit and is excluded from the analysis.

Brown et al. 2013) with an exposure time of 480 s and S/N between 11 and 49. The RV RMS is 89 m s^{-1} and the mean measurement error is 81 m s^{-1}, which is ∼2.9 times the RV semi-amplitude of TOI-622b.

2.2.2. Confirmation spectroscopy

Following the reconnaissance observations, we carried out follow-up, higher resolution and more precise spectroscopic observations of the three targets with HARPS, CORALIE, and CHIRON to determine the stellar parameters and obtain precise mass measurements. The phase-folded RVs with the best-fit model from the global analysis can be found in Fig. 1.

We collected high-resolution spectra using the High Accuracy Radial Velocity Searcher (HARPS) spectrograph under program 108.22LR.001 (PI: Psaridi) designed to specifically confirm and characterize exoplanets transiting AF-type stars. HARPS is mounted at the ESO 3.6m telescope in La Silla Observatory (Mayor et al. 2003). For several of our observations we used the HARPS high efficiency EGGS mode ($R \sim 80\,000$) which is more suitable for hot stars with high projected rotational velocities since it allows a gain of two on the throughput and provides higher RV precision for photon limited observations. By using this mode one operates at lower resolution and higher instrumental throughput when compared with standard HARPS High Accuracy Mode (HAM). We obtained 23 observations of TOI-615 from 2021 November 10 to 2022 March 23. The adopted exposure time was 1200 s which translated into a S/N between 42 and 67. A total of 16 RVs were obtained for TOI-622 from 2021 October 12 to 2022 January 04 using a median exposure time of 1800 s, resulting in a S/N range of 106 to 183. For TOI-2641 we collected six RVs from 2022 March 12 to 2022 March 22 with an exposure time of 600 s and 1800 s and S/N between 41 and 52. Additionally, nine more spectra were collected for TOI-2641 as part of the NOMADS program (PI: Armstrong, 108.21YY.001) in High-Accuracy Mode (HAM, $R \sim 115\,000$) from 2022 May 17 to 2022 May 27 with a median exposure time of 1800 s and S/N between 18 and 38. Since the HARPS observations of TOI-2641 were made under different modes they were treated as coming from independent instruments in our global analysis. The spectra were reduced with the standard calibration and reduction pipeline. The RVs were computed by cross-correlating with different binary masks

and the one that reached higher precision in the mass measurement was selected. For TOI-615, our hottest star, we used an A0 binary mask while for TOI-622 and TOI-2641 we used a G2-type binary mask. For each star, we also computed the RVs with the Fourier interspectrum method (Chelli 2000), consisting of correlating, in the Fourier space, the spectra of the star with a reference spectrum built by averaging all the spectra acquired for this star (Galland et al. 2005). The resulting RVs are consistent with those obtained with the CCF method described above. For TOI-615 one RV point (see crossed point in Fig. 1, left) was taken during transit (BJD 2459585.7779) and was affected by the Rossiter–McLaughlin (RM) effect with an expected semi-amplitude of 94 ± 12 m s^{-1}, therefore we excluded it from the analysis.

We monitored TOI-2641 with the high resolution CORALIE spectrograph that is installed at the Swiss 1.2-m *Leonhard Euler* Telescope at ESO's La Silla Observatory (Queloz et al. 2001b). CORALIE has a resolving power of R ∼ 60, 000 and is fed by a 2″ fiber (Ségransan et al. 2010). A total of 18 RVs were obtained from 2022 January 22 to 2022 March 15 using exposure times of 2400 s which translated in spectra with a signal-to-noise ratio per resolution element (S/N) between 17 and 25. We derived the RV of each epoch by cross-correlating the spectrum with a binary mask that matches the spectral type of the target (Baranne et al. 1996). The RVs of TOI-2641 were obtained using a G2 mask (Pepe et al. 2002). The bisector-span (BIS), the contrast (depth) and the full width at half-maximum (FWHM) were computed using the standard CORALIE data reduction pipeline. For each star, we also computed the RVs with the Fourier interspectrum method (see HARPS section above). These RVs are consistent with those obtained with the CCF method.

We obtained 32 spectra of TOI-2641 with the CTIO High Resolution Spectrometer (CHIRON; Tokovinin et al. 2013), a fiber-fed echelle spectrograph on the 1.5m telescope on Cerro Tololo. The spectra were collected between 2021 May 28 and 2022 December 13. The exposure time was between 1500 s or 1800 s, leading to a median S/N per extracted pixel of 20. We observed using the image slicer mode, achieving a spectral resolution of $R \sim 80\,000$, and we obtained a ThAr lamp immediately after the science exposure. The spectra were reduced using the standard CHIRON pipeline (Paredes et al. 2021), and the radial velocities were computed following the method described in Jones et al. (2019).
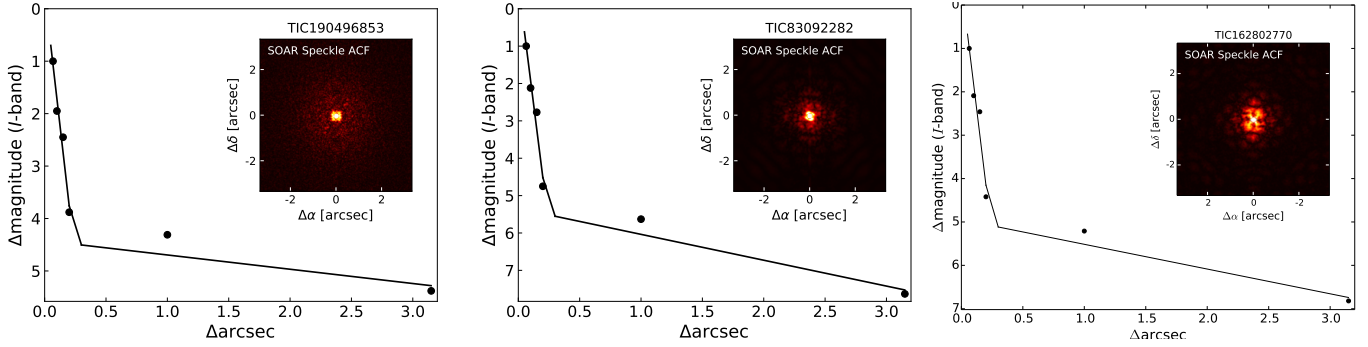
Fig. 2. SOAR speckle imaging (5σ upper limits) of TOI-615 (TIC 190496853; *left*), TOI-622 (TIC 83092282; *middle*), and TOI-2641 (TIC 162802770; *right*) that rules out stellar companions within 3 ″. The image inset represents the speckle auto-correlation function.

2.3. High resolution imaging

The large TESS pixel size (21″) can result in possible flux contamination by nearby stars. This can cause flux dilution and therefore underestimation of the observed transit depth or even false-positive transit signals. Stellar companions can be ruled out with high angular resolution imaging.

We confirmed that there are no blended companions with speckle imaging on the 4.1-m Southern Astrophysical Research (SOAR) telescope (Tokovinin 2018). The observations were taken in I-band, a similar visible bandpass as TESS. TOI-615 and TOI-622 were observed on 2019 May 18 and TOI-2641 on 2022 March 20 with no detection of nearby sources within 3″. The contrast curves with the 5σ detection limit marked with a black line are shown in Fig. 2. The inset images zoomed and centered to the targets that represent the speckle auto-correlation function do not show any stellar companions.

3. Analysis

3.1. Host star analysis

3.1.1. Spectral analysis

For the spectral analysis of TOI-615 and TOI-622 we used the coadded HARPS spectra collected in EGGS mode (PI: Psaridi, 108.22LR.001). For the analysis of TOI-2641, we used the HARPS spectra collected in the high accuracy HAM mode (PI: Armstrong, 108.21YY.001). The spectral analysis was performed using methods similar to those given in Doyle et al. (2013). The effective temperature (T_{eff}) was obtained from the excitation balance of Fe I lines and checked against that obtained from the Hα line and from fitting the spectral energy distribution. Surface gravity was determined from the ionization balance between Fe I and Fe II lines, with the Na D lines being used as a check. The iron abundance relative to Solar, [Fe/H], was obtained using the equivalent widths of the Fe lines, with a value for microturbulence taken from the calibration of Bruntt et al. (2012). The Solar abundance of iron, $\log A(\mathrm{Fe}) = 7.50$, was taken from Asplund et al. (2009).

The projected stellar rotation velocity ($v \sin i_*$) was determined by fitting the profiles of several unblended Fe I lines in the wavelength region 600–620 nm. For TOI-622 and TOI-2641 macroturbulence values of 5.9 km s^{-1} and 4.7 km s^{-1}, respectively, were obtained from the asteroseismic calibration of Doyle et al. (2014). However, TOI-615 is too hot for this calibration, so a value of 7.4 km s^{-1} was obtained by extrapolating the values given in Table B.1 of Gray (2008).

3.1.2. Spectral energy distribution

As a photometric, empirical check for consistency with the spectroscopic and model based solution of the basic stellar parameters, we performed an analysis of the broadband spectral energy distribution (SED) of each star together with the *Gaia* EDR3 parallax (with no systematic offset applied; see, e.g., Stassun & Torres 2021), in order to determine an empirical measurement of the stellar radius, following the procedures described in Stassun & Torres (2016); Stassun et al. (2017, 2018). Depending on the photometry available for each source, we pulled the $B_T V_T$ magnitudes from *Tycho*-2, the *BVgri* magnitudes from *APASS*, the JHK_S magnitudes from 2MASS, the W1–W4 magnitudes from WISE, the $GG_{BP}G_{RP}$ magnitudes from *Gaia*, and the FUV and/or NUV fluxes from GALEX. Together, the available photometry generally spans the stellar SED over the approximate wavelength range 0.2–22 μm (see Fig. 3). We performed fits to the photometry using Kurucz stellar atmosphere models, with the principal parameters being the effective temperature (T_{eff}), metallicity ([Fe/H]), and surface gravity ($\log g$), for which we adopted the spectroscopically determined values. We included the extinction, A_V, as a free parameter but limited to the full line-of-sight value from the Galactic dust maps of Schlegel et al. (1998). The resulting fits shown in Fig. 3 have a reduced χ^2 ranging from 1.1 to 1.6, and the best-fit parameters are summarized in Table 2. Integrating the model SED gives the bolometric flux at Earth, F_{bol}. Taking the F_{bol} together with the *Gaia* parallax directly gives the luminosity, L_{bol}. Similarly, the F_{bol} together with the T_{eff} and the parallax gives the stellar radius, R_*. Moreover, the stellar mass, M_*, can be estimated from the empirical eclipsing-binary based relations of Torres et al. (2010), and the (projected) rotation period can be calculated from $R_\star$ together with the spectroscopically measured $v \sin i$. When available, the GALEX photometry allows the activity index, $\log R'_{HK}$ to be estimated from the empirical relations of Findeisen et al. (2011). All quantities are summarized in Table 2.

Where possible, we have also estimated the system ages from the R'_{HK} activity and/or the stellar rotation, using the activity-age and/or rotation-age empirical relations of Mamajek & Hillenbrand (2008) which are applicable for $T_{eff} \lesssim 6500$ K. These quantities are also summarized in Table 2. Note that in the case of TOI-622, it is included in the *Gaia*-based kinematic stellar age catalog of Kounkel et al. (2020), who estimate an age of ~750 Myr, consistent with the gyrochronological age estimate. Finally, in the specific case of TOI-615 for which neither a gyrochronological age nor an activity age estimate are possible, we compare the H-R diagram position of the star to the model isochrones of Demarque et al. (2004), from

Table 2. Stellar parameters of TOI-615, TOI-622, and TOI-2641.

Property	TOI-615	TOI-622	TOI-2641	Reference
Spectral type	F2V	F6V	F9V	Pecaut & Mamajek (2013)
Identifiers				
TIC ID	190496853	83092282	162802770	TICv8
2MASS ID	J08533810-4032376	J08211322-4629031	J11243133-4243555	2MASS
Gaia ID	5524780333100885888	5516690878153930240	5382970374226953600	*Gaia* DR3
Astrometric parameters				
RA (J2000)	08:53:38.11	08:21:13.22	11:24:31.34	*Gaia* DR3
Dec (J2000)	−40:32:37.72	−46:29:03.20	−42:43:55.55	*Gaia* DR3
Parallax (mas)	2.82 ± 0.01	8.15 ± 0.01	2.88 ± 0.02	*Gaia* DR3
Distance (pc)	354.19 ± 1.71	122.69 ± 0.19	346.79 ± 2.08	*Gaia* DR3
μ_{RA} (mas yr^{-1})	-17.285 ± 0.014	-4.618 ± 0.013	-32.674 ± 0.012	*Gaia* DR3
μ_{Dec} (mas yr^{-1})	25.695 ± 0.013	-17.407 ± 0.014	-9.692 ± 0.014	*Gaia* DR3
Photometric parameters				
TESS (mag)	10.302 ± 0.006	8.562 ± 0.006	11.1897 ± 0.006	TICv8
B (mag)	11.11 ± 0.05	9.47 ± 0.03	12.02 ± 0.11	*Tycho*-2
V (mag)	10.82 ± 0.06	8.995 ± 0.002	11.69 ± 0.13	*Tycho*-2
G (mag)	10.579 ± 0.003	8.8910 ± 0.0003	11.565 ± 0.003	*Gaia* DR3
J (mag)	9.88 ± 0.02	8.11 ± 0.02	10.65 ± 0.03	2MASS
H (mag)	9.74 ± 0.03	7.93 ± 0.05	10.37 ± 0.02	2MASS
K (mag)	9.67 ± 0.02	7.86 ± 0.02	10.33 ± 0.02	2MASS
Bulk parameters				
A_V	0.15 ± 0.05	0.05 ± 0.05	0.11 ± 0.08	Sect. 3.1
F_{bol} (10^{-9} erg s^{-1} cm^{-2})	1.519 ± 0.035	6.44 ± 0.15	0.593 ± 0.028	Sect. 3.1
L_{bol} ($L_\odot$)	5.86 ± 0.14	2.979 ± 0.070	2.19 ± 0.10	Sect. 3.1
$R_\star$ ($R_\odot$)	1.732 ± 0.055	1.415 ± 0.047	1.336 ± 0.055	Sect. 3.1
$M_\star$ ($M_\odot$)	1.449 ± 0.087	1.313 ± 0.079	1.16 ± 0.07	Sect. 3.1
T_{eff} (K)	6850 ± 100	6400 ± 100	6100 ± 100	Sect. 3.1
[Fe/H] (dex)	-0.10 ± 0.07	0.09 ± 0.07	-0.15 ± 0.08	Sect. 3.1
$\log g_*$ (cm s^{-2})	4.2 ± 0.2	4.2 ± 0.2	4.2 ± 0.1	Sect. 3.1
$v \sin i_*$ (km s^{-1})	16.3 ± 0.8	19.0 ± 0.9	1.9 ± 1.2	Sect. 3.1
$P_{rot} / \sin i_*$ (days)	5.38 ± 0.31	3.77 ± 0.22	35.6 ± 13.1	Sect. 3.1
Age (Gyr)	1.7 ± 0.3	0.9 ± 0.2	10.8 ± 9.0	Sect. 3.1

Notes. The spectral type is based on the T_{eff} from the stellar analysis (see Sect. 3.1 and Table 5 in Pecaut & Mamajek 2013).
References. TICv8 (Stassun et al. 2019), 2MASS (Skrutskie et al. 2006), *Gaia* DR3 (Gaia Collaboration 2021), *Tycho*-2 (Høg et al. 2000)

which we obtain an estimated age of 1.7 ± 0.3 Gyr (see Fig. 3, upper left).

3.2. Joint transit and RV analysis

We retrieved the planet parameters using a joint photometric and RV modeling with the COde for transiting exoplaNet ANalysis (CONAN, described in Lendl et al. 2017, 2020), a Markov chain Monte Carlo (MCMC) framework. CONAN allows to jointly fit transit and RV data from different instruments while accounting for variations in the individual datasets using polynomial baseline models constructed from various external observational variables or Gaussian Processes (GPs). CONAN incorporates GPs implemented using george (Ambikasaran et al. 2015) and celerite (Foreman-Mackey et al. 2017) packages, to tackle nonwhite noise and stochastic processes in the data. The fitted parameters in the analysis are as follows: orbital period, mid-transit time, radius ratio (R_p/R_*), impact parameter, transit duration, eccentricity, argument of periastron and RV amplitude. For limb darkening, we derived quadratic coefficients and

their uncertainties for different photometric filters using the LDCU [3] routine (Deline et al. 2022). We set a Gaussian prior on the TESS limb-darkening parameters and fixed them for the ground-based photometry due to the lower precision. To account for the instrumental, atmospheric and stellar correlated noise in the ground-based light curves, we used polynomials consisting of a combination of different variables (time, stellar FWHM, airmass, coordinate shifts, and sky background). The best combination of variables favored by the Bayesian Information Criterion is selected for each dataset (Table 1). For the analysis of the TESS data, we made use of the PDCSAP fluxes that are corrected for photometric dilution from neighbor stars, therefore our model does not include a dilution factor. To account for photometric variability and additional systematics, we detrended the light curves with GP using the approximate Matérn-3/2 kernel (Foreman-Mackey et al. 2017) included in celerite package.

---

[3] https://github.com/delinea/LDCU
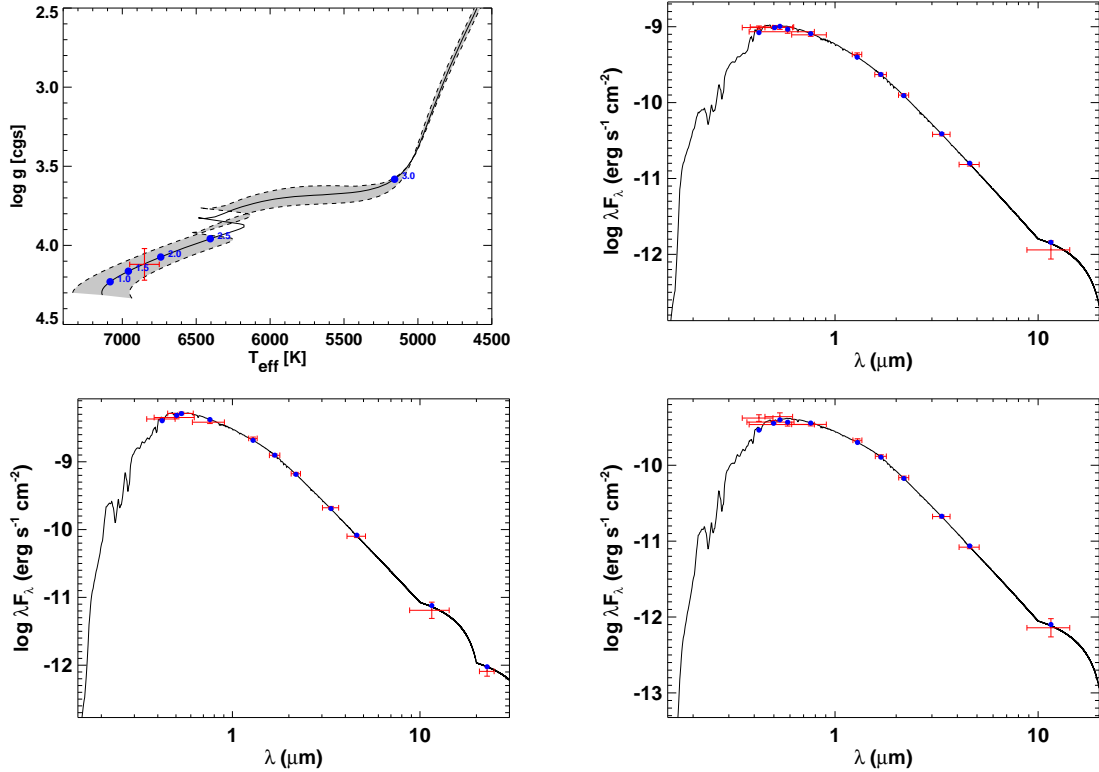
Fig. 3. Kiel diagram of TOI-615 (*upper left*) compared to model evolutionary track from Demarque et al. (2004). The red symbol represents the measured T_{eff} and $\log g$, and the shaded swathe corresponds to the uncertainties in the stellar mass and metallicity. Age points are marked in blue. Spectral energy distribution of TOI-615 (*upper right*), TOI-622 (*bottom left*), and TOI-2641 (*bottom right*). Red symbols represent the observed photometric measurements, where the horizontal bars represent the effective width of the passband. Blue symbols are the model fluxes from the best-fit Kurucz atmosphere model (black).

For the RV fitting, we ran the MCMC analysis both with the eccentricity as a free parameter and fixed to zero and found that the results are compatible with a circular orbit. Additionally, we estimated the significance of the nonzero eccentricity in order to avoid Lucy-Sweeney bias (Lucy & Sweeney 1971). Using the *F*-test approach (Lucy & Sweeney 1971) we find a 60%, 57%, and 5% probability for TOI-615, TOI-622, and TOI-2641, respectively, that the improvement in the fit could have arisen by chance if the orbit were circular. Consequently we fixed the eccentricity to zero in the global analysis. The priors used in the MCMC analysis and the posterior estimates can be found in Tables B.1 and 3, respectively.

As mentioned in Sect. 2.1.1, the V-shaped light curves of TOI-2641b suggest a grazing geometry. For the analysis, we set a broad uniform prior on the impact parameter of $\mathcal{U}(0, 1.5)$ and a large prior on R_P/R_* of $\mathcal{U}(0, 0.22)$ assuming a maximum planetary radius of $R_P < 3\ R_{Jup}$. The strong degeneracy between the impact parameter b and the companion radius R_P results in skewed posterior distributions (Fig. 4). Given this asymmetry, we extracted the best fitting values and their uncertainties using the mode (maximum value) and FWHM of each distribution. The grazing configuration results in large uncertainties on the planetary radius.

Finally, we performed a frequency analysis on the TESS light curves in order to identify stellar oscillations and retrieve the stellar rotation periods. For the analysis we made use of the TESS SAP-flux light curves and calculated the Lomb-Scargle periodograms (Lomb 1976, Scargle 1982) after masking the transit events. None of the respective periodograms revealed significant signals around the rotation periods identified by the spectral analysis.
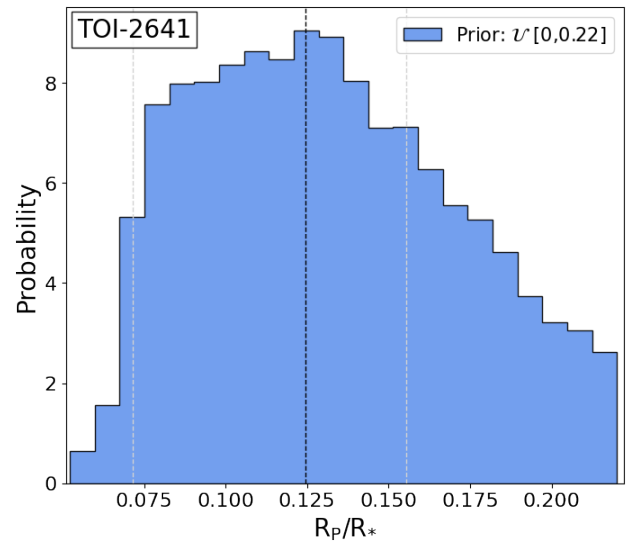
Fig. 4. CONAN posterior distribution of the R_P/R_* of TOI-2641. The black vertical line corresponds to the maximum value and the two gray vertical lines indicate the 68% credible intervals.

3.3. Planetary evolution models

Using CEPAM (Guillot & Morel 1995) and a nongray atmosphere (Parmentier et al. 2015), we model the evolution of TOI-615b, TOI-622b, and TOI-2641b. We assume simple structures consisting of a central dense core surrounded by a hydrogen and helium envelope of solar composition. The core is assumed to be composed of 50% ices and 50% rocks, by mass. Since all

Table 3. Maximum values and 68% confidence intervals of the posterior distributions from joint modeling with CONAN.

Parameters [a]	TOI-615 [b]	TOI-622 [b]	TOI-2641 [b]
Jump parameters			
P (days)	$4.6615983^{+0.0000025}_{-0.0000016}$	$6.402513^{+0.000031}_{-0.000054}$	$4.880974^{+0.000023}_{-0.000037}$
T_0 (BJD$_{\rm TDB}$)	$2459259.49383^{+0.00017}_{-0.00012}$	$2458520.69176^{+0.00031}_{-0.00046}$	$2459332.21332^{+0.00064}_{-0.00067}$
$R_{\rm P}/R_*$	$0.10023^{+0.0007}_{-0.00054}$	$0.05989^{+0.00049}_{-0.00052}$	$0.124^{+0.031}_{-0.053}$
b	$0.476^{+0.029}_{-0.068}$	$0.629^{+0.066}_{-0.091}$	$1.043^{+0.048}_{-0.065}$
T_{14} (days)	$0.1767^{+0.0011}_{-0.0011}$	$0.1628^{+0.0015}_{-0.0012}$	$0.0699^{+0.0026}_{-0.0020}$
$\sqrt{e}\sin\omega$	0	0	0
$\sqrt{e}\cos\omega$	0	0	0
ω_* (deg)	...	...	...
K (m s^{-1})	$42.4^{+6.9}_{-8.6}$	$27.8^{+6.4}_{-7.4}$	$41.6^{+2.6}_{-3.7}$
$u_{1,2\,\rm min}$	$0.209^{+0.030}_{-0.025}$	$0.226^{+0.027}_{-0.026}$	$0.274^{+0.028}_{-0.031}$
$u_{2,2\,\rm min}$	$0.349^{+0.032}_{-0.040}$	$0.287^{+0.040}_{-0.031}$	$0.322^{+0.042}_{-0.041}$
$u_{1,\rm FFI}$	$0.209^{+0.030}_{-0.025}$	...	...
$u_{2,\rm FFI}$	$0.349^{+0.032}_{-0.040}$	...	...
Derived parameters			
$R_{\rm P}$ ($R_{\rm Jup}$)	$1.693^{+0.052}_{-0.057}$	$0.824^{+0.028}_{-0.029}$	$1.615^{+0.462}_{-0.640}$
$M_{\rm P}$ ($M_{\rm Jup}$)	$0.435^{+0.086}_{-0.082}$	$0.303^{+0.069}_{-0.072}$	$0.386^{+0.022}_{-0.036}$
$\rho_{\rm P}$ ($\rho_{\rm Jup}$)	$0.084^{+0.018}_{-0.018}$	$0.507^{+0.126}_{-0.126}$	$0.092^{+0.078}_{-0.109}$
ρ (ρ_*)	$0.276^{+0.033}_{-0.030}$	$0.452^{+0.060}_{-0.047}$	$0.482^{+0.059}_{-0.060}$
e	0 (adopted, $3\sigma < 0.39$)	0 (adopted, $3\sigma < 0.42$)	0 (adopted, $3\sigma < 0.18$)
i (degrees)	$86.73^{+0.60}_{-0.22}$	$86.62^{+0.77}_{-0.54}$	$83.75^{+0.71}_{-0.55}$
a (AU)	$0.0678^{+0.0031}_{-0.0026}$	$0.0708^{+0.0052}_{-0.0059}$	$0.0607^{+0.0042}_{-0.0043}$
a/R_*	$8.458^{+0.214}_{-0.235}$	$10.637^{+0.846}_{-0.671}$	$9.677^{+0.599}_{-0.481}$
$T_{\rm eq}$ (K) [c]	1666^{+24}_{-24}	1388^{+22}_{-22}	1387^{+22}_{-23}
H (km) [c]	1601^{+332}_{-321}	454^{+108}_{-113}	1368^{+786}_{-1092}
$\langle F\rangle$ [c] (10^9 erg s^{-1} cm^{-2})	$1.75^{+0.13}_{-0.21}$	$0.82^{+0.14}_{-0.16}$	$0.82^{+0.14}_{-0.15}$
Instrumental parameters			
$\log(\sigma_{\rm w,2min})$	$-10.69^{+0.48}_{-1.22}$	$-8.65^{+0.03}_{-0.04}$	$-11.53^{+1.27}_{-0.34}$
$\log(\sigma_{\rm GP,2min})$	$-7.90^{+0.10}_{-0.18}$	$-8.65^{+0.08}_{-0.07}$	$-8.84^{+0.17}_{-0.13}$
$\log(\rho_{\rm GP,2min})$	$-0.57^{+0.12}_{-0.29}$	$-1.05^{+0.13}_{-0.10}$	$-0.90^{+0.35}_{-0.43}$
$\log(\sigma_{\rm w,FFI})$	$-11.76^{+1.26}_{-0.21}$	...	...
$\log(\sigma_{\rm w,ECAM})$	$-7.32^{+0.05}_{-0.13}$	...	$-7.83^{+0.44}_{-2.61}$
$\log(\sigma_{\rm w,NGTS_1})$	...	$-8.59^{+0.41}_{-0.20}$	...
$\log(\sigma_{\rm w,NGTS_2})$	...	$-10.42^{+0.44}_{-0.18}$	...
$\log(\sigma_{\rm w,ASTEP})$	$-7.13^{+0.11}_{-0.21}$	...	...
$\log(\sigma_{\rm w,LCO,g'})$	...	...	$-11.67^{+3.77}_{-0.15}$
$\log(\sigma_{\rm w,LCO_1(i')})$	...	...	$-11.70^{+3.08}_{-0.15}$
$\log(\sigma_{\rm w,LCO_2(i')})$	...	...	$-8.45^{+0.69}_{-3.11}$
$\log(\sigma_{\rm w,ELSAUCE})$	$-6.46^{+0.12}_{-0.11}$	...	...
$\sigma_{\rm w,HARPS1}$ [d] (km s^{-1})	$0.0222^{+0.0072}_{-0.0044}$	$0.0139^{+0.0034}_{-0.0031}$	$0.0078^{+0.0075}_{-0.0042}$
$\gamma_{\rm HARPS1}$ [d] (km s^{-1})	$31.2805^{+0.0044}_{-0.0081}$	$15.7987^{+0.0052}_{-0.0056}$	$-6.5814^{+0.0048}_{-0.0053}$
$\sigma_{\rm w,HARPS2}$ [d] (km s^{-1})	...	...	$0.0134^{+0.0094}_{-0.0063}$
$\gamma_{\rm HARPS2}$ [d] (km s^{-1})	...	...	$-6.5798^{+0.0067}_{-0.0083}$
$\sigma_{\rm w,CORALIE}$ (km s^{-1})	...	...	$0.0219^{+0.0129}_{-0.0075}$
$\gamma_{\rm CORALIE}$ (km s^{-1})	...	...	$-6.5865^{+0.0071}_{-0.0081}$
$\sigma_{\rm w,CHIRON}$ (km s^{-1})	...	...	$0.036^{+0.010}_{-0.007}$
$\gamma_{\rm CHIRON}$ (km s^{-1})	...	...	$-17.9880^{+0.0098}_{-0.0063}$

Notes. [a]The description of the parameters can be found in Table B.1. [b]The posterior estimate indicates the maximum value and then error bars the 68% credibility intervals. [c]The equilibrium temperature is calculated using $T_{\rm eq} = T_{\rm eff}(1{-}A)^{1/4}\sqrt{\frac{R_*}{2a}}$, assuming a Bond albedo of A = 0. The scale height is calculated using $H = \frac{k_{\rm b}T_{\rm eq}}{\mu g}$ assuming a mean molecular weight of 2.2 g mol^{-1}. The incident flux is calculated using $\langle F\rangle = \frac{L_*}{4\pi a^2}$. [d]HARPS^1 indicates spectra collected in EGGS mode (PI: Psaridi, 108.22LR.001) and HARPS^2 indicates spectra collected in HAM mode (PI: Armstrong, 108.21YY.001).
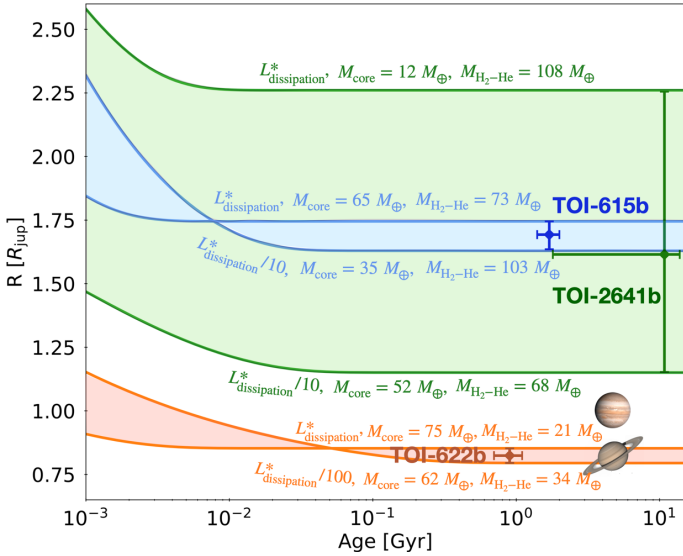
Fig. 5. Evolution models of TOI-615b, TOI-622b, and TOI-2641b. All models assume a central ice-rock core surrounded by a hydrogen-helium envelope of solar composition. Models account for dissipation of energy in the interior due to important irradiation and $L^*_{\rm dissipation}$ corresponds to our fiducial dissipation luminosity. For each planet, the ranges of core masses and envelope masses are shown. The errorbars correspond to observational constraints on their age and radius, compared to the ones of Jupiter and Saturn.

these planets are highly irradiated, we account for the dissipation of energy in the interior, following the approach of Guillot & Showman (2002): a fraction ϵ of the irradiation luminosity $L_\star$ is assumed to be dissipated at the bottom of the envelope and included in the evolution calculations.

The source and magnitude of this dissipation is still under investigation, but using a statistical approach, Thorngren & Fortney (2018) estimate for exoplanets with these irradiation levels that $\epsilon \sim 2\%$. This yields a luminosity due to internal dissipation $L^*_{\rm dissipation} = 10^{28}$, 10^{27} and 5×10^{27} erg s^{-1}, for TOI-615b, TOI-622b, and TOI-2641b respectively. In Fig. 5, we explore how observational constraints and uncertainties on dissipation affect what we can infer on the bulk composition of these planets. We show the results of calculations with our fiducial dissipation luminosity compared to models with $L^*_{\rm dissipation}$ divided by 10 (for TOI-615b and TOI-2641b) or 100 (for TOI-622b). After a few to hundred million years, our models predict that the planetary radii remain constant, due to internal heating that exceeds the planet's cooling luminosity.

We find that these planets tend to be significantly enriched in heavy elements. Defining an approximate bulk metallicity as $Z \approx M_{\rm core}/M_{\rm tot}$ and assuming $Z_\odot = 0.015$, we find $Z/Z_\odot = 17$ to 31 for TOI-615b, 43 to 52 for TOI-622b, and 7 to 29 for TOI-2641b. For comparison, Jupiter and Saturn have bulk metallicities $Z/Z_\odot$ ranging from 4 to 14, depending on assumptions on interior models (Guillot et al. 2022). For TOI-615b, and to some extent for TOI-622b, heat dissipation is found to be the dominant factor controlling the inferred composition. Spectroscopic observations of these planets (e.g., with JWST) would be highly valuable for the possibility to constrain the atmospheric metallicity and relate it to the bulk metallicity.

We also modeled the three targets using the planetary evolution code `completo21` (Mordasini et al. 2012). We used the implementation of `completo21` done by Sarkis et al. (2021). Sarkis et al. (2021) used a Bayesian framework to couple the

interior structure to the observed properties of hot-Jupiters. The planets are modeled with no central core and the heavy elements are assumed to be homogeneously mixed in the interior. The heavy elements are modeled as water with the equation of state ANEOS (Thompson 1990; Mordasini 2020) and hydrogen and helium are modeled with the SCvH equation of state (Saumon et al. 1995). The code uses a grid of fully nongray atmospheric models from `petitCODE` (Mollière et al. 2015, 2017) and the species considered are listed in Sarkis et al. (2021). We also assume that part of the stellar irradiation is transported into the planet interior. The statistical model infers the internal luminosity of the planet and thus the heating efficiency. We find an internal luminosity equal to 9×10^{27}, 7×10^{26}, and 5.5×10^{27} erg s^{-1} for TOI-615b, TOI-622b, and TOI-2641b respectively. Assuming the same stellar metallicity of $Z_\odot = 0.015$, we can derive the planet metal enrichment $Z/Z_\odot$ and find values in agreement with the ones derived with CEPAM: 19 ± 11 for TOI-615b, 43 ± 5 for TOI-622b, and 15 ± 9 for TOI-2641b. We show that considering a central core or not does not change significantly the results in terms of planet metal enrichment and both models are able to well reproduce the observed radii.

4. Discussion and conclusion

We have begun a RV survey to search for planets and brown dwarfs around AF-type stars using TESS data (Psaridi et al. 2022). As part of this survey, we present the detection and characterization of three new Saturn-mass planets that are transiting F-type stars, TOI-615b, TOI-622b, and TOI-2641b. Our analysis is based on TESS 2-min cadence and FFI data from the first 3 yr of its mission, ground-based follow-up photometry from Euler-Cam, NGTS, LCOGT, ASTEP, and El Sauce. For the analysis, we fit the photometric data jointly with RV data from HARPS, CORALIE, and CHIRON using `CONAN`.

TOI-615 and TOI-622 have effective temperatures above the Kraft break with values of $T_{\rm eff} = 6850 \pm 100$ K and $T_{\rm eff} = 6400 \pm 100$ K, respectively. Previous to our survey, only 22 Saturn-mass exoplanets (0.1–0.7 $M_{\rm Jup}$) have been confirmed to be transiting stars with $T_{\rm eff} > 6200$ K. TESS has contributed in this sample with four new detections (TOI-201b; Hobson et al. 2021, TOI-1842b; Wittenmyer et al. 2022), including TOI-615b and TOI-622b. In Fig. 6, we illustrate the planetary radius over the incident flux for all known, well-characterized transiting giant (R > 5 $R_\oplus$) planets within the mass interval 0.1–0.7 $M_{\rm Jup}$. The points are colored by the planetary mass and we highlight the planets around stars above the Kraft break in orange and the planets confirmed in this work as stars. The vertical line corresponds to the observed threshold for inflation (Demory & Seager 2011) which is based on the *Kepler* sample, showing that transiting hot Jupiters that receive a level of incident flux larger than $\sim 2 \times 10^8$ erg s^{-1} cm^{-2} (~ 146 $F_\oplus$) appear to experience radius inflation. As seen in the diagram, planets with masses in the range of ~ 0.1–0.4 $M_{\rm Jup}$, generally have radii $R < 1.5$ $R_{\rm Jup}$ while more massive planets are found to have radii as large as ~ 1.9 $R_{\rm Jup}$. This correlation between high irradiation, large mass and inflated radii has been established by Sestovic et al. (2018). The constrained masses and radii of TOI-615b, TOI-622b, and TOI-2641b follow this correlation.

With a mass of 0.44 ± 0.08 $M_{\rm Jup}$ and a radius of 1.69 ± 0.05 $R_{\rm Jup}$, TOI-615b has a density of 0.119 ± 0.026 g cm^{-3} (~ 0.09 $\rho_{\rm Jup}$), thus it is ranked among the 2% lowest density, well-characterized known planets and it the least-dense planet discovered with TESS. Moreover, TOI-615b is the lowest density
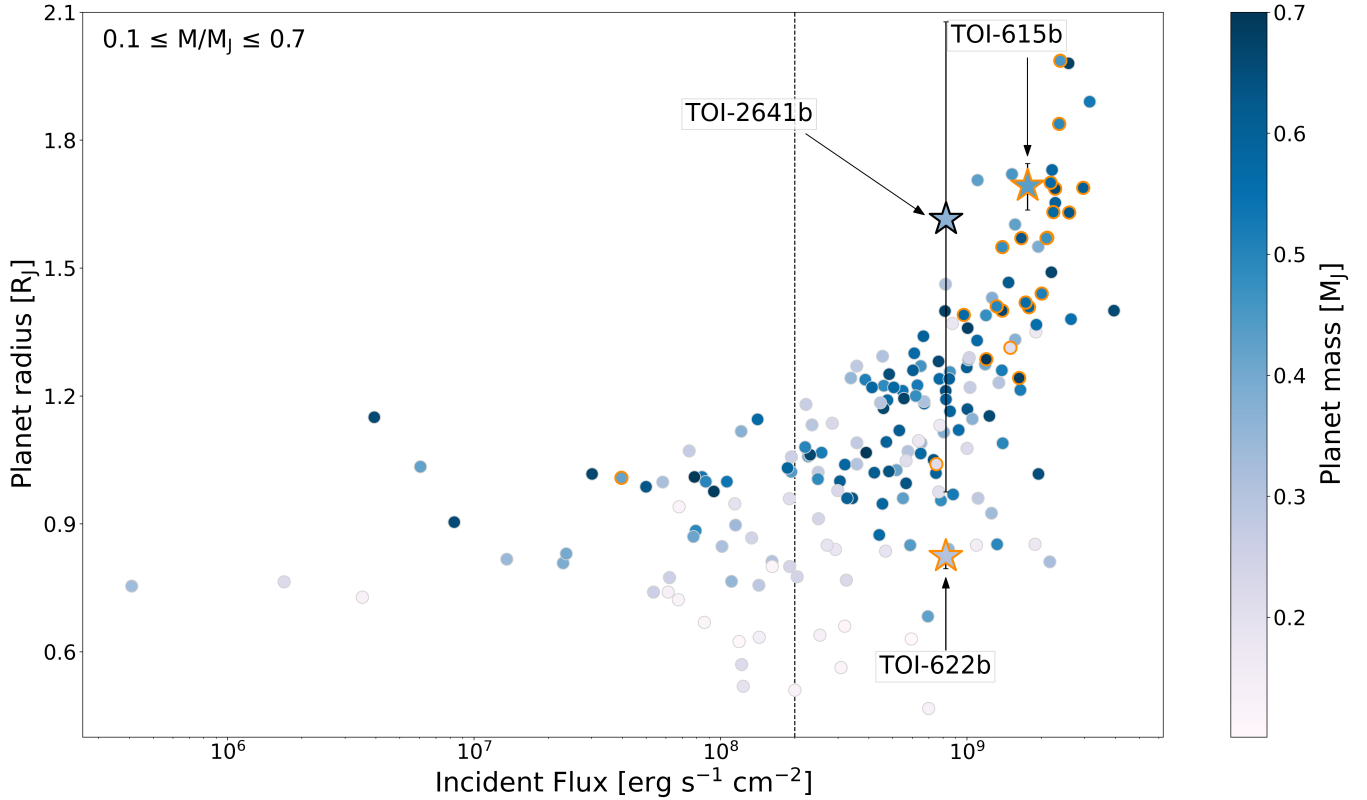
Fig. 6. Planet radius over incident flux for known giant ($R > 5\,R_\oplus$) planets within the mass interval 0.1–0.7 $M_{\rm Jup}$. The points are colored by the planetary mass. The vertical dashed line corresponds to the planetary inflation threshold (146 $F_\oplus$, Demory & Seager 2011). Stars with effective temperatures above the Kraft break are outlined in orange. The three new planets, TOI-615b, TOI-622b, and TOI-2641b, have been highlighted as stars and labeled.

planet that transits a star with such high effective temperature ($T_{\rm eff} = 6850 \pm 100\,{\rm K}$). Placing TOI-615b on the radius-incident flux diagram (Fig. 6) we see that the planet is among the largest hot Saturns known. We calculate the incident flux received by TOI-615b to be $\sim 1.75 \times 10^9$ erg s^{-1} cm^{-2} ($\sim 1277\,F_\oplus$) which is one order of magnitude larger than the insolation threshold for inflation. Using the Weiss et al. (2013) empirical relationship for predicted radius of planets with $M_{\rm P} < 150\,M_\oplus$ ($M_{\rm P} < 0.47\,M_{\rm Jup}$) that makes use of the planetary mass and incident flux:

$$\frac{R_{\rm P}}{R_\oplus} = 1.78 \left(\frac{M_{\rm P}}{M_\oplus}\right)^{0.53} \left(\frac{F}{\text{erg s}^{-1}\ \text{cm}^{-2}}\right)^{-0.03}$$

we predict a planetary radius of $12.8 \pm 1.3\,R_\oplus$. With a measured radius of $18.6 \pm 0.6\,R_\oplus$, TOI-615b appears to be inflated by $\sim 45\%$.

In contrast to TOI-615b, TOI-622b with a mass of $0.29 \pm 0.07\,M_{\rm Jup}$ and a radius of $0.83 \pm 0.03\,R_{\rm Jup}$ is unusually dense with a density of 0.718 ± 0.181 g cm^{-3} ($\sim 0.52\,\rho_{\rm Jup}$). TOI-622b receives an incident flux of $\sim 8.2 \times 10^8$ erg s^{-1} cm^{-2} ($\sim 600\,F_\oplus$) which is well above the lower inflation limit, however, the planet does not show evidence of inflation. TOI-622b has a predicted planetary radius of $10.8 \pm 1.3\,R_\oplus$; its observed radius of $9.04 \pm 0.31\,R_\oplus$ is thus slightly smaller (1.3σ) than expected.

TOI-2641b is a $0.39 \pm 0.04\,M_{\rm Jup}$ hot Jupiter with a poorly constrained radius ($1.61^{+0.46}_{-0.64}\,R_{\rm Jup}$) due to the extremely grazing nature of the transit with impact parameter of $b = 1.042^{+0.048}_{-0.065}$. The V-shaped transits obtained by TESS, EulerCam, and LCOGT can be seen in Fig. A.1. As shown in Fig. 6, TOI-2641b receives 613 times more incident flux than Earth. Given its mass

and insolation, we do not expect TOI-2641b to have a radius larger than $\sim 1.5\,R_{\rm Jup}$. This planet adds to the population of grazing planets ($b + R_{\rm p}/R_* \geq 1$) with 19 confirmed detections to-date. These targets have sensitive transit depth and duration which makes them promising for long term monitoring in searches for additional planets through TTVs and TDVs (Ribas et al. 2008).

As discussed in Sect. 3.2, we modeled all three systems assuming a circular orbit. We estimated the circularization timescales using equation 3 of Adams & Laughlin (2006) for tidal quality factor $Q_{\rm p} = 10^5$ and 10^6. TOI-615b might have circularized after $0.021^{+0.008}_{-0.007}$ Gyr for $Q_{\rm p} = 10^5$ and $0.21^{+0.08}_{-0.07}$ Gyr for $Q_{\rm p} = 10^6$, which is shorter than the lifetime of the system (1.7 ± 0.3 Gyr). For TOI-622b the expected circularization timescale is $0.81^{+0.46}_{-0.51}$ Gyr using $Q_{\rm p} = 10^5$ and $8.1^{+4.6}_{-5.1}$ Gyr using $Q_{\rm p} = 10^6$. Compared to the age of the host star (0.9 ± 0.2 Gyr), TOI-622b might have undergone tidal circularization or formed in situ in a nearly circular orbit. Finally, the expected tidal circularization timescale of TOI-2641b is $0.016^{+0.024}_{-0.016}$ Gyr for $Q_{\rm p} = 10^5$ and $0.16^{+0.24}_{-0.16}$ Gyr for $Q_{\rm p} = 10^6$ which is significantly shorter than the estimated stellar age (10.8 ± 9.0 Gyr). This is consistent with TOI-2641b having undergone circularization before reaching its present age.

Winn et al. (2010) noted that planets orbiting stars with effective temperatures above the Kraft break have a higher probability to be in a polar or retrograde orbit. In fact, 20 out of the 35 planets on misaligned orbits ($|\lambda| > 10°$, with $> 3\sigma$ confidence) have been found to orbit hot stars (Fig. 7). Studies of the projected spin-orbit angle of can bring essential insights on the formation processes and migration of planets transiting massive, early-type stars. Given the high effective temperature, the

large planetary radius and high stellar rotational velocity, TOI-615 and TOI-622 are very appealing systems for future RM effect observations (Rossiter 1924; McLaughlin 1924). We predict the semi-amplitude of the RM effect for each planet by using Eq. (1) in Triaud (2018). For TOI-615b, the expected semi-amplitude of the RM signal is $A_{RM} = 92 \pm 10$ m s^{-1} and for TOI-622 $A_{RM} = 142 \pm 20$ m s^{-1}. As discussed in Sect. 2.2.2, one data point of TOI-615 occurred during transit and was affected by the RM effect with a semi-amplitude of 94 ± 12 m s^{-1} providing weak constrain on the orbital obliquity.

The large predicted signals of TOI-615 and TOI-622 suggest that the targets are good candidates for such observations. As the RM technique relies on isolating the stellar signal emanating from the regions occulted by the planets, grazing transits are suboptimal for exploiting the RM effect. Plus, the majority of the techniques employed to analyze this effect (e.g., velocimetry, Ohta et al. 2005; Doppler tomography, Gandolfi et al. 2012) assume that the successive occulted stellar profiles are constant during the transit, which naturally biases the derived parameters (Cegla et al. 2016, Bourrier et al. 2017) even in fiducial cases. This assumption is all the less justifiable in case of a grazing transit and would accentuate those biases. Consequently, such studies could be challenging for TOI-2641.

Due to the high equilibrium temperature of the planets, we investigate the possibility of future atmospheric studies via transmission spectroscopy. Figure 7 shows the expected transmission spectral signal of 1 atmospheric scale height (H, assuming a mean molecular weight of 2.2 g mol^{-1}) approximated by Bento et al. (2014):

$$A_{\mathrm{abs}} = \frac{2R_{\mathrm{p}}H}{R_{\star}^2} \qquad (1)$$

as a function of the stellar effective temperature for exoplanets with well-constrained densities. The expected absorption signals are: 261^{+59}_{-58} ppm, 54^{+13}_{-14} ppm, 358^{+309}_{-354} ppm for TOI-615b, TOI-622b, and TOI-2641b respectively. Figure 7 locates TOI-615b in the 2% of planets with highest A_{abs} that makes it an ideal candidate for future atmospheric studies. Additionally, observations with the *James Webb* Space Telescope (JWST) can allow the comparison of planets that suffer from extreme stellar irradiation to cooler gas giants. For that purpose, we calculate the Transmission Spectroscopy Metric (TSM, Kempton et al. 2018) that corresponds to the expected transmission spectroscopy signal-to-noise ratio (S/N). A higher TSM implies easier determination of the planet's atmospheric spectrum. We computed the TSM from Kempton et al. (2018):

$$\mathrm{TSM} = S \times \frac{R_{\mathrm{P}}^3 T_{\mathrm{eq}}}{M_{\mathrm{P}} R_*^2} \times 10^{-m_{\mathrm{J}}/5}, \qquad (2)$$

where m_{J} is the apparent magnitude of the star in the J band. The scale factor (S) depends on the planetary radius as: $S = 0.19$ for $R_{\mathrm{P}} < 1.5\ R_{\oplus}$; $S = 1.26$ for $1.5 < R_{\mathrm{P}} < 2.75\ R_{\oplus}$; $S = 1.28$ for $2.75 < R_{\mathrm{P}} < 4.0\ R_{\oplus}$ and $S = 1.15$ for $4.0 < R_{\mathrm{P}} < 10\ R_{\oplus}$. For TOI-615b and TOI-2641b we adopted a scale factor $S = 1$ since their radii are larger than $10\ R_{\oplus}$. For TOI-615b we calculate a value of TSM = 286 ± 19, for TOI-622b TSM = 203 ± 14, and for TOI-2641b TSM = 351^{+303}_{-351}. According to Table 1 from Kempton et al. (2018), TOI-615b and TOI-622b are ranked in the first quartile, and hence they have beneficial properties for follow-up atmospheric characterization through transmission spectroscopy with JWST with TOI-615b being especially promising.
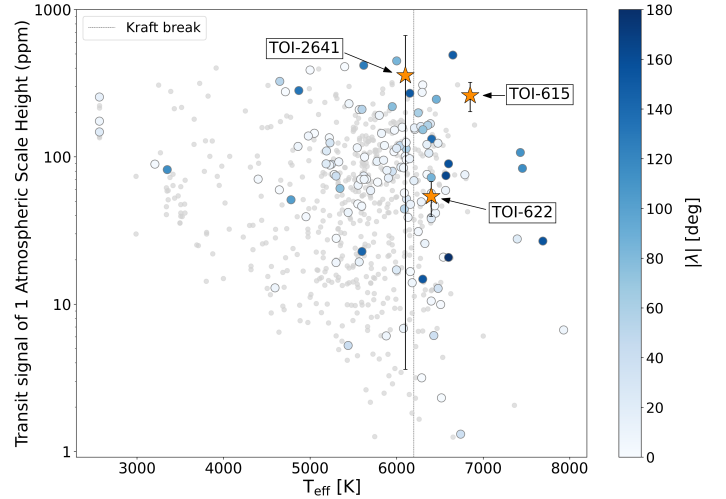
Fig. 7. Expected transmission spectral signal of 1 atmospheric scale height (Bento et al. 2014) versus stellar effective temperature for exoplanets with precise densities ($\sigma_{\mathrm{M}}/M \leq 25\%$ and $\sigma_{\mathrm{R}}/R \leq 8\%$). The points of planets with Rossiter-McLaughlin (RM) observations are color-coded with the absolute value of their sky-projected spin-orbit angle ($|\lambda|$). The three new planets, TOI-615b, TOI-622b, and TOI-2641b, have been highlighted as orange stars and labeled.

References

Abe, L., Gonçalves, I., Agabi, A., et al. 2013, A&A, 553, A49
Adams, F. C., & Laughlin, G. 2006, ApJ, 649, 1004
Addison, B., Wright, D. J., Wittenmyer, R. A., et al. 2019, PASP, 131, 115003
Addison, B. C., Knudstrup, E., Wong, I., et al. 2021, AJ, 162, 292
Ambikasaran, S., Foreman-Mackey, D., Greengard, L., Hogg, D. W., & O'Neil, M. 2015, IEEE Trans. Pattern Anal. Mach. Intell., 38, 252
Asplund, M., Grevesse, N., Sauval, A. J., & Scott, P. 2009, ARA&A, 47, 481
Baranne, A., Queloz, D., Mayor, M., et al. 1996, A&AS, 119, 373
Barbary, K. 2016, J. Open Source Softw., 1, 58
Bento, J., Wheatley, P. J., Copperwheat, C. M., et al. 2014, MNRAS, 437, 1511
Bertin, E., & Arnouts, S. 1996, A&AS, 117, 393
Borucki, W. J., Koch, D., Basri, G., et al. 2010, Science, 327, 977
Bourrier, V., Cegla, H. M., Lovis, C., & Wyttenbach, A. 2017, A&A, 599, A33
Brahm, R., Nielsen, L. D., Wittenmyer, R. A., et al. 2020, AJ, 160, 235
Brown, T. M., Baliber, N., Bianco, F. B., et al. 2013, PASP, 125, 1031
Bruntt, H., Basu, S., Smalley, B., et al. 2012, MNRAS, 423, 122
Bryant, E. M., Bayliss, D., McCormac, J., et al. 2020, MNRAS, 494, 5872
Cegla, H. M., Oshagh, M., Watson, C. A., et al. 2016, ApJ, 819, 67
Chelli, A. 2000, A&A, 358, L59
Collins, K. A., Kielkopf, J. F., Stassun, K. G., & Hessman, F. V. 2017, AJ, 153, 77
Collins, K. A., Quinn, S. N., Latham, D. W., et al. 2018, AAS Meeting, 231, 439.08
Deline, A., Hooton, M. J., Lendl, M., et al. 2022, A&A, 659, A74
Demarque, P., Woo, J.-H., Kim, Y.-C., & Yi, S. K. 2004, ApJS, 155, 667
Demory, B.-O., & Seager, S. 2011, ApJS, 197, 12
Dong, J., Huang, C. X., Zhou, G., et al. 2021, ApJ, 920, L16
Doyle, A. P., Smalley, B., Maxted, P. F. L., et al. 2013, MNRAS, 428, 3164
Doyle, A. P., Davies, G. R., Smalley, B., Chaplin, W. J., & Elsworth, Y. 2014, MNRAS, 444, 3592
Findeisen, K., Hillenbrand, L., & Soderblom, D. 2011, AJ, 142, 23
Foreman-Mackey, D., Agol, E., Ambikasaran, S., & Angus, R. 2017, AJ, 154, 220
Gaia Collaboration (Brown, A. G. A., et al.) 2018, A&A, 616, A1
Gaia Collaboration (Brown, A. G. A., et al.) 2021, A&A, 649, A1
Galland, F., Lagrange, A.-M., Udry, S., et al. 2005, A&A, 443, 337
Gandolfi, D., Collier Cameron, A., Endl, M., et al. 2012, A&A, 543, A5
Gray, D. F. 2008, The Observation and Analysis of Stellar Photospheres (Cambridge, UK: Cambridge University Press)
Guerrero, N. M., Seager, S., Huang, C. X., et al. 2021, ApJS, 254, 39
Guillot, T., & Morel, P. 1995, A&AS, 109, 109
Guillot, T., & Showman, A. P. 2002, A&A, 385, 156
Guillot, T., Abe, L., Agabi, A., et al. 2015, Astronomische Nachrichten, 336, 638
Guillot, T., Fletcher, L. N., Helled, R., et al. 2022, ArXiv e-prints, [arXiv:2205.04100]
Hobson, M. J., Brahm, R., Jordán, A., et al. 2021, AJ, 161, 235
Høg, E., Fabricius, C., Makarov, V. V., et al. 2000, A&A, 355, A27
Huang, C. X., Vanderburg, A., Pál, A., et al. 2020, Res. Notes AAS, 4, 204
Ikwut-Ukwa, M., Rodriguez, J. E., Quinn, S. N., et al. 2022, AJ, 163, 9
Jenkins, J. M. 2002, ApJ, 575, 493
Jenkins, J. M., Chandrasekaran, H., McCauliff, S. D., et al. 2010, SPIE Conf. Ser., 7740, 77400D

Jenkins, J. M., Twicken, J. D., McCauliff, S., et al. 2016, SPIE Conf. Ser., 9913, 99133E
Jenkins, J. M., Tenenbaum, P., Seader, S., et al. 2020, Kepler Data Processing Handbook: Transiting Planet Search, Kepler Science Document KSCI-19081-003, 9
Jensen, E. 2013, Astrophysics Source Code Library [record ascl:1306.007]
Jones, M. I., Brahm, R., Espinoza, N., et al. 2019, A&A, 625, A16
Jordán, A., Brahm, R., Espinoza, N., et al. 2020, AJ, 159, 145
Kabáth, P., Chaturvedi, P., MacQueen, P. J., et al. 2022, MNRAS, 513, 5955
Kempton, E. M. R., Bean, J. L., Louie, D. R., et al. 2018, PASP, 130, 114401
Kossakowski, D., Espinoza, N., Brahm, R., et al. 2019, MNRAS, 490, 1094
Kounkel, M., Covey, K., & Stassun, K. G. 2020, AJ, 160, 279
Kovács, G., Zucker, S., & Mazeh, T. 2002, A&A, 391, 369
Kraft, R. P. 1967, ApJ, 150, 551
Lendl, M., Anderson, D. R., Collier-Cameron, A., et al. 2012, A&A, 544, A72
Lendl, M., Cubillos, P. E., Hagelberg, J., et al. 2017, A&A, 606, A18
Lendl, M., Bouchy, F., Gill, S., et al. 2020, MNRAS, 492, 1761
Li, J., Tenenbaum, P., Twicken, J. D., et al. 2019, PASP, 131, 024506
Lomb, N. R. 1976, Ap&SS, 39, 447
Lucy, L. B., & Sweeney, M. A. 1971, AJ, 76, 544
Mamajek, E. E., & Hillenbrand, L. A. 2008, ApJ, 687, 1264
Mayor, M., Pepe, F., Queloz, D., et al. 2003, The Messenger, 114, 20
McCully, C., Volgenau, N. H., Harbeck, D.-R., et al. 2018, SPIE Conf. Ser., 10707, 107070K
McLaughlin, D. B. 1924, ApJ, 60, 22
Mékarnia, D., Guillot, T., Rivet, J. P., et al. 2016, MNRAS, 463, 45
Mollière, P., van Boekel, R., Dullemond, C., Henning, T., & Mordasini, C. 2015, ApJ, 813, 47
Mollière, P., van Boekel, R., Bouwman, J., et al. 2017, A&A, 600, A10
Mordasini, C. 2020, A&A, 638, A52
Mordasini, C., Alibert, Y., Klahr, H., & Henning, T. 2012, A&A, 547, A111
Ohta, Y., Taruya, A., & Suto, Y. 2005, ApJ, 622, 1118
Otegi, J. F., Bouchy, F., & Helled, R. 2020, A&A, 634, A43
Paredes, L. A., Henry, T. J., Quinn, S. N., et al. 2021, AJ, 162, 176
Parmentier, V., Guillot, T., Fortney, J. J., & Marley, M. S. 2015, A&A, 574, A35
Pecaut, M. J., & Mamajek, E. E. 2013, ApJS, 208, 9
Pepe, F., Mayor, M., Rupprecht, G., et al. 2002, The Messenger, 110, 9
Psaridi, A., Bouchy, F., Lendl, M., et al. 2022, A&A, 664, A94
Queloz, D., Henry, G. W., Sivan, J. P., et al. 2001a, A&A, 379, 279
Queloz, D., Mayor, M., Udry, S., et al. 2001b, The Messenger, 105, 1
Ribas, I., Font-Ribera, A., & Beaulieu, J.-P. 2008, ApJ, 677, L59
Ricker, G. R., Winn, J. N., Vanderspek, R., et al. 2015, J. Astron. Telescopes Instrum. Syst., 1, 014003
Rodriguez, J. E., Quinn, S. N., Zhou, G., et al. 2021, AJ, 161, 194
Rodriguez, J. E., Quinn, S. N., Vanderburg, A., et al. 2023, MNRAS, 521, 2765
Rossiter, R. A. 1924, ApJ, 60, 15
Sarkis, P., Mordasini, C., Henning, T., Marleau, G. D., & Mollière, P. 2021, A&A, 645, A79
Saumon, D., Chabrier, G., & van Horn, H. M. 1995, ApJS, 99, 713
Scargle, J. D. 1982, ApJ, 263, 835
Schlegel, D. J., Finkbeiner, D. P., & Davis, M. 1998, ApJ, 500, 525
Ségransan, D., Udry, S., Mayor, M., et al. 2010, A&A, 511, A45
Sestovic, M., Demory, B.-O., & Queloz, D. 2018, A&A, 616, A76
Siverd, R. J., Brown, T. M., Barnes, S., et al. 2018, SPIE Conf. Ser., 10702, 107026C
Skrutskie, M. F., Cutri, R. M., Stiening, R., et al. 2006, AJ, 131, 1163
Smith, J. C., Stumpe, M. C., Van Cleve, J. E., et al. 2012, PASP, 124, 1000
Smith, A. M. S., Eigmüller, P., Gurumoorthy, R., et al. 2020, Astron. Nachr., 341, 273
Sozzetti, A., Damasso, M., Bonomo, A. S., et al. 2021, A&A, 648, A75
Stassun, K. G., & Torres, G. 2016, AJ, 152, 180
Stassun, K. G., & Torres, G. 2021, ApJ, 907, L33
Stassun, K. G., Collins, K. A., & Gaudi, B. S. 2017, AJ, 153, 136
Stassun, K. G., Corsaro, E., Pepper, J. A., & Gaudi, B. S. 2018, AJ, 155, 22
Stassun, K. G., Oelkers, R. J., Paegert, M., et al. 2019, AJ, 158, 138
Stumpe, M. C., Smith, J. C., Van Cleve, J. E., et al. 2012, PASP, 124, 985
Stumpe, M. C., Smith, J. C., Catanzarite, J. H., et al. 2014, PASP, 126, 100
Thompson, S. L. 1990, ANEOS analytic equations of state for shock physics codes input manual, Tech. Rep. https://doi.org/10.2172/6939284
Thorngren, D. P., & Fortney, J. J. 2018, AJ, 155, 214
Tokovinin, A. 2018, PASP, 130, 035002
Tokovinin, A., Fischer, D. A., Bonati, M., et al. 2013, PASP, 125, 1336
Torres, G., Andersen, J., & Giménez, A. 2010, A&ARv, 18, 67
Triaud, A. H. M. J. 2018, in Handbook of Exoplanets, eds. H. J. Deeg, & J. A. Belmonte, 2
Twicken, J. D., Catanzarite, J. H., Clarke, B. D., et al. 2018, PASP, 130, 064502
Ulmer-Moll, S., Lendl, M., Gill, S., et al. 2022, A&A, 666, A46
Vanzi, L., Zapata, A., Flores, M., et al. 2018, MNRAS, 477, 5041

Wang, S., Jones, M., Shporer, A., et al. 2019, AJ, 157, 51
Weiss, L. M., Marcy, G. W., Rowe, J. F., et al. 2013, ApJ, 768, 14
Wheatley, P. J., West, R. G., Goad, M. R., et al. 2018, MNRAS, 475, 4476
Winn, J. N., Fabrycky, D., Albrecht, S., & Johnson, J. A. 2010, ApJ, 718, L145
Wittenmyer, R. A., Clark, J. T., Trifonov, T., et al. 2022, AJ, 163, 82
Wong, I., Shporer, A., Zhou, G., et al. 2021, AJ, 162, 256
Yee, S. W., Winn, J. N., Hartman, J. D., et al. 2022, AJ, 164, 70
Yee, S. W., Winn, J. N., Hartman, J. D., et al. 2023, ApJS, 265, 1

[1] Observatoire de Genève, Université de Genève, Chemin Pegasi 51, 1290 Versoix, Switzerland
e-mail: angeliki.psaridi@unige.ch

[2] Vanderbilt University, Department of Physics & Astronomy, 6301 Stevenson Center Lane, Nashville, TN 37235, USA

[3] Astrophysics Group, Keele University, Staffordshire ST5 5BG, UK

[4] Department of Physics, University of Warwick, Gibbet Hill Road, Coventry CV4 7AL, UK

[5] Centre for Exoplanets and Habitability, University of Warwick, Gibbet Hill Road, Coventry CV4 7AL, UK

[6] Université Côte d'Azur, Observatoire de la Côte d'Azur, CNRS, Laboratoire Lagrange, Bd de l'Observatoire, CS 34229, 06304 Nice cedex 4, France

[7] Physikalisches Institut, University of Bern, Gesellschaftsstrasse 6, 3012 Bern, Switzerland

[8] Astrobiology Research Unit, Université de Liège, 19C Allée du 6 Août, 4000 Liège, Belgium

[9] Department of Earth, Atmospheric and Planetary Science, Massachusetts Institute of Technology, 77 Massachusetts Avenue, Cambridge, MA 02139, USA

[10] Instituto de Astrofísica de Canarias (IAC), Calle Vía Láctea s/n, 38200 La Laguna, Tenerife, Spain

[11] Center for Data Intensive and Time Domain Astronomy, Department of Physics and Astronomy, Michigan State University, East Lansing, MI 48824, USA

[12] Mullard Space Science Laboratory, University College London, Holmbury St Mary, Dorking, Surrey RH5 6NT, UK

[13] El Sauce Observatory, Río Hurtado, Coquimbo Province, Chile

[14] University of Southern Queensland, Centre for Astrophysics, West Street, Toowoomba, QLD 4350, Australia

[15] Department of Astrophysical Sciences, Princeton University, Princeton, NJ 08544, USA

[16] Center for Astrophysics | Harvard & Smithsonian, 60 Garden Street, Cambridge, MA 02138, USA

[17] University of Grenoble Alpes, CNRS, IPAG, 38000 Grenoble, France

[18] Instituto de Astrofísica e Ciências do Espaço, Universidade do Porto, CauP, Rua das Estrelas, 4150-762 Porto, Portugal

[19] Department of Physics, Engineering and Astronomy, Stephen F. Austin State University, 1936 North St, Nacogdoches, TX 75962, USA

[20] Department of Physics and Kavli Institute for Astrophysics and Space Research, Massachusetts Institute of Technology, Cambridge, MA 02139, USA

[21] Department of Aeronautics and Astronautics, Massachusetts Institute of Technology, Cambridge, MA 02139, USA

[22] SETI Institute, 189 Bernardo Ave, Suite 200, Mountain View, CA 94043, USA

[23] Facultad de Ingeniera y Ciencias, Universidad Adolfo Ibáñez, Av. Diagonal las Torres 2640, Peñalolén, Santiago, Chile

[24] Millennium Institute for Astrophysics, Faculty of Physics, Campus San Joaquin UC, Av. Vicuna Mackenna, 4860, Mascul, Santiago, Chile

[25] Data Observatory Foundation, Eliodoro Yáñez, 2990, Providencia, Santiago, Chile

[26] European Southern Observatory, Alonso de Córdova 3107, Vitacura, Casilla, 19001, Santiago, Chile

[27] NASA Ames Research Center, Moffett Field, CA 94035, USA

[28] Swinburne University of Technology, Centre for Astrophysics and Supercomputing, John Street, Hawthorn, VIC 3122, Australia

[29] Cerro Tololo Inter-American Observatory/NSF's NOIRLab, Casilla 603, La Serena, Chile

[30] Astrophysics Group, Cavendish Laboratory, J.J. Thomson Avenue, Cambridge, CB3 0HE, UK

[31] George Mason University, 4400 University Drive, Fairfax, VA 22030, USA

[32] Department of Extrasolar Planets and Atmospheres, Institute of Planetary Research, German Aerospace Center (DLR), Rutherford-straße 2, 12489 Berlin, Germany

[33] Bryant Space Science Center, Department of Astronomy, University of Florida, Gainesville, FL 32611, USA

[34] University of Maryland, Baltimore County, Baltimore, MD 21250, USA

[35] NASA Goddard Space Flight Center, 8800 Greenbelt Rd, Greenbelt, MD 20771, USA

[36] Space Research Institute, Austrian Academy of Sciences, Schmiedl-straße 6, 8042 Graz, Austria

[37] Department of Physics and Astronomy, The University of North Carolina at Chapel Hill, Chapel Hill, NC 27599-3255, USA

[38] European Southern Observatory, Karl-Schwarzschild-Strae 2, 85748 Garching bei München, Germany

[39] South African Astronomical Observatory, PO Box 9, Observatory, Cape Town 7935, South Africa

[40] School of Physics & Astronomy, University of Birmingham, Edgbaston, Birmingham B15 2TT, UK

[41] Department of Electrical Engineering and Center of Astro Engineering, Pontificia Universidad Católica de Chile, Av. Vicuña Mackenna 4860, Santiago, Chile

[42] Departamento de Astronomia, Universidad de Chile, Casilla 36-D, Santiago, Chile

[43] Astrophysics Research Centre, Queen's University Belfast, Belfast BT7 1NN, UK

Appendix A: Light curves
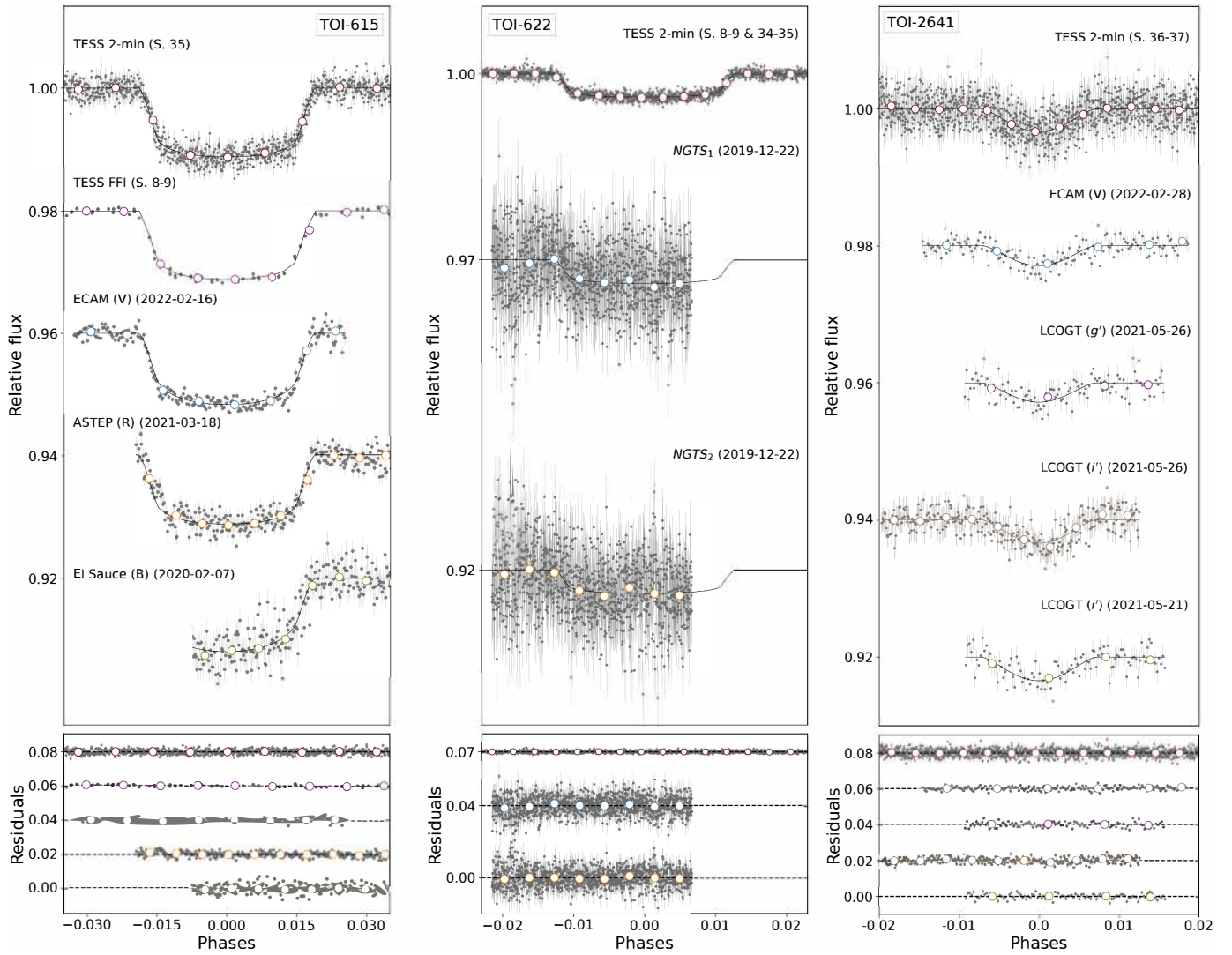
Fig. A.1: Phase-folded detrended TESS, EulerCam, ASTEP, EL-Sauce, NGTS, and LCOGT light curves for TOI-615b (*left*), TOI-622b (*middle*), and TOI-2641b (*right*). The model plotted is the MCMC best-fit solution to the global model.

Appendix B: Joint analysis priors

Table B.1: Prior values for the joint photometric and radial velocity analysis of TOI-615, TOI-622, and TOI-2641 with CONAN.

Parameters	TOI-615	TOI-622	TOI-2641
P (days), orbital period	$\mathcal{U}(4.5, 4.8)$	$\mathcal{U}(6.2, 6.6)$	$\mathcal{U}(4.6, 5.0)$
T_0 (BJD$_{TDB}$), time of conjunction	$\mathcal{U}(2459258, 2459260)$	$\mathcal{U}(2458520, 2458521)$	$\mathcal{U}(2459332, 2459333)$
R_P/R_*, planet-to-star radius	$\mathcal{U}(0, 0.2)$	$\mathcal{U}(0, 0.2)$	$\mathcal{U}(0, 0.22)$
b, impact parameter	$\mathcal{U}(0, 1)$	$\mathcal{U}(0, 1)$	$\mathcal{U}(0, 1.5)$
e, eccentricity	$\mathcal{F}(0)$	$\mathcal{F}(0)$	$\mathcal{F}(0)$
ω_* (deg), argument of periastron	...	...	...
K (ms^{-1}), RV semi-amplitude	$\mathcal{U}(10, 60)$	$\mathcal{U}(10, 40)$	$\mathcal{U}(10, 60)$
TESS photometry:			
$\log(\sigma_{w,2min})$, jitter	$\mathcal{U}(-12, -5)$	$\mathcal{U}(-12, -5)$	$\mathcal{U}(-12, -5)$
$\log(\sigma_{GP,2min})$, amplitude of the GP	$\mathcal{U}(-10, 5)$	$\mathcal{U}(-10, 5)$	$\mathcal{U}(-10, 5)$
$\log(\rho_{GP,2min})$, time/length-scale of the GP	$\mathcal{U}(-3, 3)$	$\mathcal{U}(-3, 3)$	$\mathcal{U}(-5, 5)$
$\log(\sigma_{w,FFI})$, jitter	$\mathcal{U}(-12, -5)$	...	...
$u_{1,2min}$, limb-darkening coefficient	$\mathcal{N}(0.201, 0.040)$	$\mathcal{N}(0.239, 0.034)$	$\mathcal{N}(0.257, 0.034)$
$u_{2,2min}$, limb-darkening coefficient	$\mathcal{N}(0.321, 0.044)$	$\mathcal{N}(0.314, 0.041)$	$\mathcal{N}(0.298, 0.039)$
$u_{1,FFI}$, limb-darkening coefficient	$\mathcal{N}(0.201, 0.040)$	...	...
$u_{2,FFI}$, limb-darkening coefficient	$\mathcal{N}(0.321, 0.044)$	...	...
Ground based photometry:			
$u_{1,ECAM}$, limb-darkening coefficient	$\mathcal{F}(0.379)$	...	$\mathcal{F}(0.443)$
$u_{2,ECAM}$, limb-darkening coefficient	$\mathcal{F}(0.311)$	...	$\mathcal{F}(0.286)$
$\log(\sigma_{w,ECAM})$, jitter	$\mathcal{U}(-12, -5)$	...	$\mathcal{U}(-12, -5)$
$u_{1,NGTS_{1,2}}$, limb-darkening coefficient	...	$\mathcal{F}(0.289)$	...
$u_{2,NGTS_{1,2}}$, limb-darkening coefficient	...	$\mathcal{F}(0.316)$	...
$\log(\sigma_{w,NGTS_{1,2}})$, jitter	...	$\mathcal{U}(-12, -5)$	...
$u_{1,ASTEP}$, limb-darkening coefficient	$\mathcal{F}(0.251)$	...	...
$u_{2,ASTEP}$, limb-darkening coefficient	$\mathcal{F}(0.331)$	...	...
$\log(\sigma_{w,ASTEP})$, jitter	$\mathcal{U}(-12, -5)$	...	...
$u_{1,LCO,g'}$, limb-darkening coefficient	...	...	$\mathcal{F}(0.547)$
$u_{2,LCO,g'}$, limb-darkening coefficient	...	...	$\mathcal{F}(0.217)$
$\log(\sigma_{w,LCO,g'})$, jitter	...	...	$\mathcal{U}(-12, -5)$
$u_{1,LCO_{1,2}(i')}$, limb-darkening coefficient	...	...	$\mathcal{F}(0.259)$
$u_{2,LCO_{1,2}(i')}$, limb-darkening coefficient	...	...	$\mathcal{F}(0.298)$
$\log(\sigma_{w,LCO_{1,2},i'})$, jitter	...	...	$\mathcal{U}(-12, -5)$
$u_{1,ELSAUCE}$, limb-darkening coefficient	$\mathcal{F}(0.511)$	...	...
$u_{2,ELSAUCE}$, limb-darkening coefficient	$\mathcal{F}(0.269)$	...	...
$\log(\sigma_{w,ELSAUCE})$, jitter	$\mathcal{U}(-12, -5)$	...	...
Radial velocities:			
γ_{HARPS^1} (km s^{-1}), systemic RV	$\mathcal{U}(30, 33)$	$\mathcal{U}(14, 16)$	$\mathcal{U}(-8, -5)$
$\sigma_{w,HARPS^1}$ (km s^{-1}), jitter	$\mathcal{U}(0, 100)$	$\mathcal{U}(0, 100)$	$\mathcal{U}(0, 100)$
γ_{HARPS^2} (km s^{-1}), systemic RV	...	...	$\mathcal{U}(-8, -5)$
$\sigma_{w,HARPS^2}$ (km s^{-1}), jitter	...	...	$\mathcal{U}(0, 100)$
$\gamma_{CORALIE}$ (km s^{-1}), systemic RV	...	...	$\mathcal{U}(-8, -5)$
$\sigma_{w,CORALIE}$ (km s^{-1}), jitter	...	...	$\mathcal{U}(0, 100)$
γ_{CHIRON} (km s^{-1}), systemic RV	...	...	$\mathcal{U}(-19, -16)$
$\sigma_{w,CHIRON}$ (km s^{-1}), jitter	...	...	$\mathcal{U}(0, 100)$

Notes. [a] For the priors, $\mathcal{N}(\mu, \sigma^2)$ indicates a normal distribution with mean μ and variance σ^2, $\mathcal{U}(a, b)$ a uniform distribution between a and b, $\log\mathcal{U}(a, b)$ a log-uniform distribution between a and b and $\mathcal{F}(a)$ a parameter fixed to value a.
[b] HARPS[1] indicates spectra collected in EGGS mode (PI: Psaridi, 108.22LR.001) and HARPS[2] indicates spectra collected in HAM mode (PI: Armstrong, 108.21YY.001).